Tomography analysis of the intermediate-luminosity Type Iax SN 2024pxl

Barnabás Barna[1,2], Mridweeka Singh[3], Lindsey A. Kwok[4] ⋆, Saurabh W. Jha[5], R. Dastidar[6], Conor Larison[5], Alexei V. Filippenko[7], J. P. Anderson[8], Jennifer E. Andrews[9], Moira Andrews[10,11], G. C. Anupama[12], Prasiddha Arunachalam[13], Katie Auchettl[14,14], Dominik Bánhidi[1,15], K. Azalee Bostroem[16] ⋆⋆, Thomas G. Brink[7], Régis Cartier[17], Ping Chen[18,19], T.-W. Chen[20], Collin T. Christy[16], David A. Coulter[21], Sofia Covarrubias[22], Kyle W. Davis[13], Connor B. Dickinson[13], Yize Dong[23], Joseph Farah[10,11], Andreas Flörs[24], Ryan J. Foley[13], Noah Franz[16], Christoffer Fremling[22,25], Lluís Galbany[26,27], Anjasha Gangopadhyay[28], Aarna Garg[13], Elinor L. Gates[29], Or Graur[30,31], Mariusz Gromadzki[32], Daichi Hiramatsu[23,33], Emily Hoang[34], D. Andrew Howell[10,11], Brian Hsu[16], Joel Johansson[35], Arti Joshi[36], Lordrick A. Kahinga[13], Ravjit Kaur[13], Sahana Kumar[37], Piramon Kumnurdmanee[13], Hanindyo Kuncarayakti[38,39], Chang Liu[4,40], Keiichi Maeda[41], Kate Maguire[42], Bailey Martin[43], Curtis McCully[10,11], Darshana Mehta[34], Luca M. Menotti[13], Anne J. Metevier[44], A. A. Miller[4,33,45], Kuntal Misra[46], Erika Mochnács[1], T. E. Müller-Bravo[42,47], Megan Newsome[10,48], Estefania Padilla Gonzalez[49], Kishore C. Patra[13], Jeniveve Pearson[16], Anthony L. Piro[50], Abigail Polin[51], Aravind P. Ravi[35], Armin Rest[21,49], Nicolas Meza Retamal[35], O. M. Robinson[13], César Rojas-Bravo[52,53], Devendra K. Sahu[12], David J. Sand[16], Brian P. Schmidt[43], Steve Schulze[4], Michaela Schwab[5], Manisha Shrestha[16], Matthew R. Siebert[21], Sunil Simha[4,54], Nathan Smith[16], Jesper Sollerman[28], Shubham Srivastav[55], Bhagya M. Subrayan[16], Tamás Szalai[1,56], Kirsty Taggart[13], Rishabh Singh Teja[12], Jacco H. Terwel[42], Samaporn Tinyanont[57], Stefano Valenti[35], József Vinkó[1,48,58,59], Aya L. Westerling[13], J. Craig Wheeler[48], Yi Yang[7,60], and WeiKang Zheng[7]

(Affiliations can be found after the references)

Received September 30, 20XX

ABSTRACT

We present an abundance tomography analysis of SN 2024pxl, an intermediate luminosity Type Iax supernova ($M_{\mathrm{r}} = -16.82 \pm 0.19$ mag), with the most-detailed follow-up in the Type Iax subclass to-date. As one of the few intermediate luminosity Type Iax objects, SN 2024pxl may link the two extremes of the peculiar thermonuclear supernova subclass. To test this hypothesis, we analyze its spectral evolution through the first 100 days after the explosion and aim to probe the structure of its ejecta. We conduct an abundance tomography analysis using synthetic spectra produced with the one dimensional radiative transfer code TARDIS. The fit of the spectral time series provides a radial scan of physical properties and probes the stratification of chemical elements throughout most of the SN ejecta. The observed spectral evolution is well fit with the final model, similar to the general predictions of the pure deflagration scenarios, but significant modifications are required in the density function of the inner ejecta and in the chemical profiles of the outermost regions. The constrained physical characteristics, such as the photospheric velocities and the time of maximum light, are also consistent with other SNe Iax. Despite their small number, intermediate luminosity Type Iax SNe are not outliers in the subclass but demonstrate the continuous nature of SNe Iax through their luminosity range. Following this observation, we argue that all SNe Iax share the same progenitor and explosion origin.

1. Introduction

Type Iax supernovae (SNe Iax) form one of the most numerous subclasses of white dwarf (WD) explosions. Their estimated rate for all WD SNe varies between 5 and 30% based on different volume-limited samples (Dimitriadis et al. 2025; Foley et al. 2013, respectively). The main properties of SNe Iax are their relatively low-luminosity, along with other peculiar characteristics of a low-energy thermonuclear explosion. Unlike other subclasses of SNe Ia, the Iax group exhibits great diversity in all of these properties. The peak absolute magnitudes range from −18.6 mag (SN 2011ay; Szalai et al. 2015) to −12.6 mag (SN 2021fcg; Karambelkar et al. 2021) in the r/R-band, while the expansion velocities of the photosphere span from ~2000 (SN 2008ha; Foley et al. 2009) to ~9000 km s^{-1} (SN 2012Z; Stritzinger et al. 2015) at the moment of maximum light. Spectroscopically, SNe Iax are similar to "normal" SNe Ia at early epochs, although the well-known features of intermediate mass elements (IMEs), such as the Ca II H&K or the Si II λ6355 lines, are less prominent. At the same time, features of iron group elements (IGEs), such as the regions around 4100 and 5200 Å formed by Fe II, are dominant from the first days indicating the presence of IGEs in the outer layers of the SN ejecta. SNe Iax never turn fully nebular at later epochs; instead, they show permitted P Cygni and forbidden emission lines simultaneously, even years after the explosion (Camacho-Neves et al. 2023). The blackbody emitting source required by this phenomenon can be explained via a bound remnant, which is formed from the burned material falling back due to the insufficient kinetic energy that failed to fully unbind the progenitor WD.

The most promising explosion scenario, the so-called pure or "failed" deflagration (Jordan et al. 2012; Kromer et al. 2013) can explain both the relatively low luminosities and the low kinetic

⋆ CIERA Fellow
⋆⋆ LSST-DA Catalyst Fellow

energies. All published hydrodynamic models (Jordan et al. 2012; Kromer et al. 2013; Long et al. 2014; Fink et al. 2014; Kromer et al. 2015; Leung & Nomoto 2020; Lach et al. 2022) predict spherically symmetric ejecta, with a uniform abundance structure due to heavy mixing. The nearly constant mass fractions of chemical elements, dominated by unburned material (C and O from the WD) and IGEs, can successfully reproduce the observed spectral evolution in general (see e.g. Kwok et al. 2025) around and after maximum (i.e., over the majority of the ejecta), even at extremely late epochs, which probe the innermost regions of SNe Iax (Camacho-Neves et al. 2023). The assumption of completely uniform ejecta has been questioned by both the locations of line forming regions (Stritzinger et al. 2015) and abundance tomography analyzes (Barna et al. 2018, 2021a; Singh et al. 2023, 2024; Barna et al. 2026). However, the signs of a stratified abundance structure are limited to early epochs, and thus, the outer regions of the ejecta.

State-of-the-art pure deflagration models of C/O WDs can only account for the relatively luminous (RL, with a peak absolute magnitude of $M_r < -17$ mag) and intermediate luminosity (IL, with $-17 < M_r < -14.5$ mag) cases of the SN Iax class. For the extremely low-luminosity group (EL, $M_r > -14.5$ Barna et al. 2026), the only plausible solution so far has been the deflagration of a hybrid C/O/Ne WD (Meng & Podsiadlowski 2014). Kromer et al. (2015) presented hydrodynamic simulations that reproduced the main observables of the prototype object SN 2008ha ($M_R = -14.3$, Foley et al. 2009). The lack of a general explanation for the explosion scenario of the EL sample, including the even less luminous objects discovered since SN 2008ha (e.g. SNe 2019gsc, 2021fcg, 2024vjm; Tomasella et al. 2020; Srivastav et al. 2020; Karambelkar et al. 2021; Zimmerman et al. 2026), has raised the question of whether SNe Iax indeed form a few-parameter family (Barna et al. 2018) or can be distinguished into two (or more) subclasses with distinct observables and/or origins (Singh et al. 2023). To resolve this question, the slowly growing IL sample is of great importance, as these transitional objects can constrain the continuous nature of SNe Iax over the entire luminosity range.

SN 2024pxl is only the third IL SN Iax with a multi-wavelength photometric dataset and spectral series, after SNe 2019muj (Barna et al. 2021a) and 2022xlp (Bánhidi et al. 2025). The study of these objects may link the two extremes of SNe Iax, assuming that the physical properties change continuously through the luminosity range of the subclass. The follow-up of SN 2024pxl provided the most detailed dataset of the subclass, both in the covered time period and wavelength range. The monitoring of the SN started just a few days after the explosion and continued for an unprecedented late +500 days. While it was observed by Swift, the Hubble Space Telescope, and numerous ground-based telescopes, SN 2024pxl was also the first SN Iax that was targeted by the James Webb Space telescope with NIRSpec and MIRI detectors (Kwok et al. 2025). The analysis of the emission lines at near- and mid-infrared wavelengths (NIR and MIR) provided constraints on the symmetry and uniformity of the ejecta. All these factors made SN 2024pxl the most well-observed and, simultaneously, one of the most important objects in the Iax subclass. After detailed photometric and spectroscopic studies (Hoogendam et al. 2025; Kwok et al. 2025; Singh et al. 2026), we aim to reconstruct the properties of the ejecta via abundance tomography to complete its analysis.

The paper is organized as follows. Section 2 summarizes the published results regarding SN 2024pxl and the observed datasets. Section 3 presents the abundance tomography, including the description of the radiative transfer code TARDIS and the adopted fitting strategy. The results of the analysis are presented in Section 4, while the main conclusions are summarized in Section 5.

2. SN 2024pxl

SN 2024pxl was discovered by the `BTSbot` machine-learning model (Rehemtulla et al. 2024) at 60514.4 MJD using observations from the Zwicky Transient Facility (ZTF, Graham et al. 2019). Its host galaxy, NGC 6384, is a spiral galaxy at a redshift of $z = 0.0056$, and has been the subject of several distance measurements over the last two decades. Most of these estimates were obtained via the Tully-Fisher method, with results varying between 18.7 and 29.7 Mpc. As the most recent estimate, Singh et al. (2026) presented a light curve analysis of the Type Ia SN 2017dh, which exploded close to the center of NGC 6384. The well-sampled $BgVri$ photometry was fitted with the BayeSN code (Thorp et al. 2021; Mandel et al. 2022) and constrained its distance to $d = 23 \pm 2.0$ Mpc (assuming $H_0 = 73$ km s^{-1} Mpc^{-1}). This value is consistent with both previous results and matches well with that of Cosmicflow-3 ($d = 25.1 \pm 4.0$ Mpc), the latest Tully-Fisher study (Tully et al. 2016).

The observed spectra of SN 2024pxl suffered significant reddening. Schlafly & Finkbeiner (2011) estimated $E(B-V)_{MW} = 0.11$ mag as the Milky Way extinction in the direction of NGC 6384. The host galaxy reddening is constrained based on the narrow Na I D features by Singh et al. (2026), because the lines at the redshift of NGC 6384 have similar widths to those at Milky Way wavelengths. Thus, the total reddening is assumed to be $E(B-V) = 0.22$ mag. Note that this value of extinction might still be underestimated, as the slope of the early spectral continuum falls short of that of SNe 2019muj and 2022xlp, two Type Iax SNe with similar peak absolute magnitudes (see Fig. 1). However, the redder continuum of SN 2024pxl could be due to intrinsic properties as well.

Table 1. Observables and estimated light curve properties of SN 2024pxl adopted from Singh et al. (2026).

Host Galaxy	NGC 6384
redshift	0.0056
distance [Mpc]	23.0 ± 2.0
distance modulus [mag]	31.81 ± 0.11
$E(B-V)_{MW}$ [mag]	0.11
$E(B-V)_{host}$ [mag]	0.11
T_{first} [MJD]	60513.9 ± 0.1
T_{max} in V-band [MJD]	60526.9 ± 0.5
T_{max} in r-band [MJD]	60527.6 ± 0.5
$M_V(max)$ [mag]	−16.58 ± 0.19
$M_r(max)$ [mag]	−16.82 ± 0.19

The peak absolute magnitudes are $M_V = -16.6$ mag and $M_r = -16.8$ mag (Singh et al. 2026), which place SN 2024pxl in the intermediate luminous (IL) group of the Type Iax class. Due to its transitional luminosity and proximity, SN 2024pxl became an ideal target for a follow-up campaign. Right after its discovery, high-cadence optical monitoring commenced, resulting in the most detailed photometric and spectroscopic dataset of a Type Iax SN. The ground-based data were collected and published by Singh et al. (2026), where the authors performed light curve analysis (including the estimation of peak properties, the time of first light, and decline rates), constructed and studied the bolometric light curve, and compared the spectral evolution of SN 2024pxl to that of other SNe Iax. In Table 1 we summarize the main observables of SN 2024pxl as published by Singh et al. (2026).

SN 2024pxl was selected for target of opportunity observations with the James Webb Space Telescope and became the first Type Iax SN observed with the Near-Infrared Spectrograph (NIRSpec) and the Mid-Infrared Instrument (MIRI). The four spectral epochs presented by Kwok et al. (2025) sampled the panchromatic evolution between +11 and +40 days with respect to *r* band maximum, allowing for the study of the simultaneously present photospheric and nebular lines. The analysis of the forbidden lines showed similar and centrally symmetric line profiles for all identified elements, indicating a uniform chemical distribution.

In this study, we use the published spectral series of Singh et al. (2026) and also adopt the estimated date of maximum light ($T_{\max}$ = 60527.6 ± 0.5 MJD in the *r* band) as the reference time. The detailed description and log of observations can be found in Singh et al. (2026); here, Table 2 only lists those spectra that were adopted for spectral synthesis in our study. One spectrum is obtained with the Double Beam Spectrograph (DBSP; Oke & Gunn 1982) from Palomar Observatory, with the Robert Stobie Spectrograph (RSS) of the Southern African Large Telescope (SALT), with the Kast double spectrograph at Lick Observatory, and with the Low Resolution Imaging Spectrometer (LRIS; Oke et al. 1995) on the Keck I telescope. Two epochs were observed with the Alhambra Faint Object Spectrograph and Camera (ALFOSC) mounted on the Nordic Optical Telescope (NOT), and four epochs were acquired through the Global Supernova Project (GSP) collaboration using the telescopes of Las Cumbres Observatory (LCO; Brown et al. 2013). These spectra are chosen to sample the ejecta almost uniformly: the time intervals are shorter at earlier epochs when the photospheric velocity is expected to decrease rapidly, while the sampling becomes less frequent when the spectral evolution slows down. Additionally, two yet unpublished spectra are also involved in the analysis, which were obtained by the ePESSTO+ project (Smartt et al. 2015) with the ESO Faint Object Spectrograph and Camera version 2 (EFOSC2; Buzzoni et al. 1984) at the 3.6-m New Technology Telescope (NTT) are used here. The epochs of SN 2024pxl chosen for this study sample the first 100 days after the explosion. All spectra are scaled to photometry using polynomial functions and dereddened for the total assumed reddening of $E(B - V) = 0.22$ mag.

3. Abundance tomography

Abundance tomography analysis is a powerful technique for studying expanding ejecta. As the SN expands, the photosphere recedes, allowing the observer to see deeper into the ejecta. The new layers contributing to the spectrum are denser and thus predominantly affect the formation of the spectral lines at a certain epoch. By fitting the spectral time series with the same ejecta model, we can map both the physical properties and the abundance of line forming elements layer by layer.

Since the first abundance tomography study of SN 2002bo (Stehle et al. 2005), only a handful of objects have been analyzed using this method. Mapping the distribution of the chemical elements provided an effective tool to distinguish between the various explosion scenarios; thus, tomography analysis was adopted for multiple thermonuclear SNe: the well-observed normal Type Ia SNe 2011fe (Mazzali et al. 2014, 2015) and 2014J (Ashall et al. 2014), the transitional Type Ia SN 2021rhu (Harvey et al. 2023), the subluminous SN 1986G (Ashall et al. 2016), the super-Chandra SN 2009dc (Hachinger et al. 2012), and 1991T-like SNe (Sasdelli et al. 2014; O'Brien et al. 2024). The method was also used to constrain the IGE abundances in outer layers, which have a particular impact on the observed UV fluxes (Hachinger et al. 2013; Barna et al. 2021b). However, the broad and often saturated absorption features of SNe Ia increase the degeneracy of spectral fits and thus limit the accuracy of the inferred ejecta models. Type Iax supernovae exhibit more numerous and narrower spectral lines, significantly increasing both the number and quality of the fitting constraints. To date, 16 of these subluminous events, ~13% of the discovered Iax population, have been the subject of abundance tomography analysis. The full list and references of the objects can be found in Table A.1. All of the spectral synthesis of these tomography analyzes was performed with the 1D Monte Carlo-based radiative transfer code TARDIS (Kerzendorf & Sim 2014).

TARDIS provides robust tracking of photon propagation in a homologously expanding atmosphere, which allows for obtaining reliable ejecta properties even with the computational power of a desktop PC. The code also allows for the design of SN ejecta by defining the densities and chemical composition of radial layers; thus, it provides a powerful tool to synthesize and fit SN spectra. Here we use the v2025.10.12 release of the radiative transfer code TARDIS (Kerzendorf et al. 2025). The code assumes radially symmetric ejecta with a sharp blackbody emitting photosphere and follows the propagation of photon packets through the predefined layers via Monte Carlo simulations. Multiple options are available for light-matter interaction, excitation, and ionization rates. The chosen options and the convergence strategy of the TARDIS model runs are presented in Appendix A.2, while the fitting strategy is described in Sec. 3.

In this study, we aim to constrain the mass fraction of twelve chemical elements, assuming a non-uniform distribution. We chose the seven most abundant elements (O, C, Si, S, Fe, Co, Ni) of the *N1def* model and five additional elements (namely Ca, Mg, Ti, V, Cr), whose line formation impact has been previously identified in Type Iax spectra by abundance tomography studies. The abundance of every other chemical element is fixed at the same value as in the N1def model (Fink et al. 2014), which has been shown to provide a solid match with the spectral features of SN 2024pxl (Kwok et al. 2025). In the case of mass fraction deficit, we choose oxygen as the "filler" element for normalization, since its spectral lines are well distinguished and the overestimation of its mass fraction does not spoil the fits. We define radial layers with velocity steps of 1000 km s^{-1}, in which we fit the mass fraction of the chemical elements. This choice is necessary to test the possible stratification of the ejecta, but it provides a large number of free parameters, which is unsuitable for exploring the entire parameter space. Instead, we set all mass fractions to a constant value representing the general abundances of the N1def model as an initial guess and alter the mass fraction of any layers if the fit of a spectral feature requires it. Note that this fitting strategy is not aimed at finding the best-fit synthetic spectra (even though we use the term "best-matching" in the following for simplification); rather, it is intended to provide a plausible solution for the ejecta model.

We adopt a density formula similar to that of Barna et al. (2021a), which contains an exponential inner part and a shallow

Table 2. Log of the spectra of SN 2024pxl involved in the abundance tomography analysis.

Date	MJD	t_{exp} [d]	Phase [d]	Telescope/Instrument	Wavelength range [Å]
2024-07-24	60515.34	4.6	−8.8	P200/DBSP	3400 - 10500
2024-07-26	60517.45	6.7	−6.7	FTN/FLOYDS	3500 - 10000
2024-07-28	60519.26	8.5	−4.9	FTN/FLOYDS	3500 - 10000
2024-07-30	60521.79	11.1	−2.3	SALT/RSS	3500 - 9400
2024-08-02	60524.69	14.0	+0.6	Lick/Kast	3600 - 10700
2024-08-05	60527.29	16.6	+3.2	FTN/FLOYDS	3500 - 10000
2024-08-10	60532.97	22.3	+8.9	NOT/ALFOSC	3500 - 9800
2024-08-18	60540.32	29.6	+16.2	FTN/FLOYD	3500 - 10000
2024-08-31	60553.04	42.3	+28.9	NTT/EFOSC2	3650 - 9250
2024-09-08	60561.05	50.3	+36.9	NTT/EFOSC2	3650 - 9250
2024-09-21	60574.86	64.1	+50.75	NOT/ALFOSC	3500 - 9650
2024-10-30	60613.20	103.5	+89.09	Keck/LRIS	3650 - 10000

Notes. t_{exp} shows the time since the date of explosion constrained in the abundance tomography (MJD 60510.9); while the phases are given relative to the maximum in r-band (MJD 60527.6).

cut-off toward higher velocities:

$$\rho(v, t_{exp}) = \begin{cases} \rho_0 \cdot \left(\frac{t_{exp}}{t_0}\right)^{-3} \cdot \exp\left(-\frac{v}{v_0}\right) & \text{for } v \leq v_{cut} \\ \rho_0 \cdot \left(\frac{t_{exp}}{t_0}\right)^{-3} \cdot \exp\left(-\frac{v}{v_0}\right) \cdot C^{-\frac{(v-v_{cut})^2}{v_{cut}^2}} & \text{for } v > v_{cut} \end{cases} \quad (1)$$

where v is the velocity coordinate, ρ_0 is the core density (i.e., density at $v = 0$ km s^{-1}) at the reference time t_0; v_0 defines the decline rate of the exponential density profile; v_{cut} marks the start of the rapid decline of the outer regions, and C scales the strength of the cut-off. Eq. 1 can effectively reproduce the density profiles of pure deflagration models (for an example, see Fig. 4). To reduce the number of free parameters, we fix the strength of the cut-off as $C = 8.2 \times 10^5$, which produces a similar decline in the density function to that of the N1def model. The v_{cut} can be adjusted by the widths of the strongest absorption features, such as the Fe II lines between 4500 and 5200 Å both before and after maximum light. Fitting the blue wings of these lines indicates a velocity shift of ∼6500 km s^{-1}, which is adopted for v_{cut} in the whole abundance tomography. Note that during the abundance tomography, the core of the ejecta is not covered; thus, ρ_0 cannot be constrained directly, and it acts as a simple scaling factor for the density profile. Moreover, the ρ_0 and v_0 parameters are strongly coupled because a spectral epoch samples only a short range of the whole ejecta, and the layers have continuously lower impact outward in the SN atmosphere. To handle the degeneracy between the parameters of Eq. 1, we fix the slope of the exponential function to $v_0 = 3000$ km s^{-1}, which has already provided plausible solutions for the spectral synthesis of similar Type Iax SNe such as SNe 2015H and 2022xlp ($M_r = -17.27$ and -16.06, Magee et al. 2016; Bánhidi et al. 2025, respectively). The date of the explosion is fit by assuming that the moment of first-light ($T_{first} = 60513.86 \pm 0.10$ MJD, Singh et al. 2026) adopted from the LC analysis works as an upper limit. Luminosities and photospheric velocities are constrained individually for each spectrum.

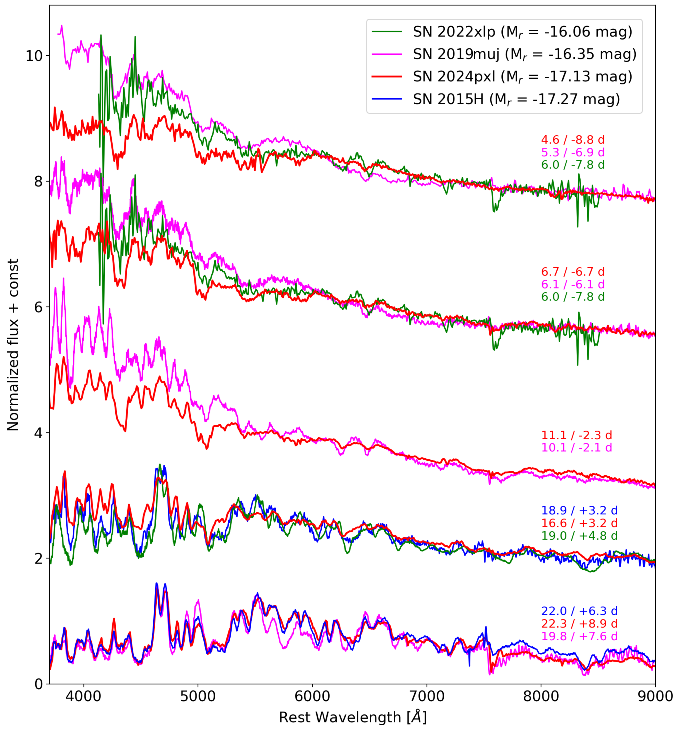

Fig. 1. The comparison of early spectral evolution of SN 2024pxl (red) with that of a less luminous SNe 2019muj and 2022xlp (Barna et al. 2021a; Bánhidi et al. 2025, magenta and green, respectively) and the more luminous SN 2015H (Magee et al. 2016, blue) SNe Iax. The listed epochs show the time since explosion / the time since the r band maximum in days.

4. Results

The TARDIS radiative transfer code and the fitting strategy described in Sec. 3 were proven to be effective methods for synthesizing the spectral evolution of SN 2024pxl. TARDIS becomes less reliable with time after maximum light for normal SNe Ia because it works in the optically thick regime. However, it can be used for SNe Iax even at late epochs due to the existence of a continuum emitting photosphere possibly originating from a bound remnant (Foley et al. 2016; Camacho-Neves et al. 2023). As presented in Figs. 2 and 3, both the continuum in general and most of the P Cygni lines are reproduced with the same ejecta model over 100 days of evolution.

The evolved spectral features of the first spectrum (60515.34 MJD; $t_{exp} = 4.6$ days), such as the two Fe II dominated regions around 4300 and 5400 Å, and the lack of a visible Si II λ6345 line, indicate that the photosphere has already reached the denser region of the ejecta but is still relatively hot, as assumed by the required excitation temperatures. These characteristics constrain the epoch to 4-6 days after the explosion, according to the analysis of other SNe Iax. The direct comparison of SN 2024pxl to its closest relatives by luminosity, SNe 2015H and 2019muj (see Fig. 1), by peak luminosity ($M_r = -17.27$ and -16.35 mag, respectively), also supports this estimation of the time since explosion (t_{exp}).

The density structure of the N1def model used as an initial guess had to be reduced, as the fits of lines at near- and post-maximum epochs required lower densities by an order of magnitude. The final model was constructed with a core density of $\rho_0 = 0.2$ g cm^{-3} (at the reference time of $t_{exp} = 100$ s), determined by the form of Eq. 1. This produces densities close to the photosphere (in the most impactful line forming region) at the latest epochs that were an order of magnitude lower than those of the N1def model. These modifications also allowed for a realistic result for the date of explosion, which, based on the fits of the first two epochs, is constrained to $T_{exp} = 60510.7$ MJD with an approximate uncertainty of 1.5 days. Although a "dark phase" (Piro & Nakar 2013, 2014) between the moment of explosion and the first observed light ($T_{first} = 60513.9$ MJD) is expected, the difference of ~ 3.2 days marks a significant discrepancy.

The assumption of a sharp photosphere is robust throughout the studied time period. The location of the inner boundary of the ejecta, i.e., the velocity of the photosphere (v_{phot}), affects not only the blueshift of multiple P Cygni features but also has a significant impact on the temperature profile of the SN atmosphere and, thus, on the ionization/excitation relations. More specifically, the fit of the thinner lines (such as Ni II λ4068, the S II W-feature, C II λ6580) and the relative strengths of Fe II and Fe III features between 4500-5200 Å are effective ways to constrain v_{phot} before and around maximum light. At later epochs, v_{phot} was mainly estimated from modeling the shape of the continuum flux (via T_{phot}) and the shift of several strong Fe II lines (see Fig. 3).

The complex impact on the synthetic spectrum allows v_{phot} to be set with sufficient precision of a few hundred km s^{-1} in the abundance tomography analysis. The time function of v_{phot} (the inferred values are presented in Fig. 6) declines rapidly at the earliest epochs, showing a nearly linear trend around maximum light, and slowly flattens during late-time. This resembles that of normal SNe Ia, with the difference being a non-ceasing photospheric phase.

The best-matching chemical abundances are shown in Fig. 5. Similar to other studies of SNe Iax, the outermost layers - sampled by the first epochs - cannot be described well with a uniform structure. As presented in Fig. 2, both C, IMEs (e.g., Si) and IGEs (e.g., Fe and ^{56}Ni) would produce overwhelmingly strong and blueshifted lines if the initial abundance structure of the N1def model is kept. Instead, these elements are introduced in the best-matching model with increasing mass fractions in the deeper layers revealed at subsequent epochs. The outermost region over 6000 km s^{-1} is dominated by C and O, representing the unburned material of the progenitor WD. While oxygen is used as a filler element in general, and thus its abundance is overestimated (see the misfit of the O I λ7779 line), the carbon mass fraction is estimated according to the fit of C II λ6580 and is also constrained by the barely detectable C III λ4647 line. As a further discrepancy from the uniform abundance scheme of the deflagration model, carbon is limited to being present above 7000 km s^{-1} in the final TARDIS model because even a few per-

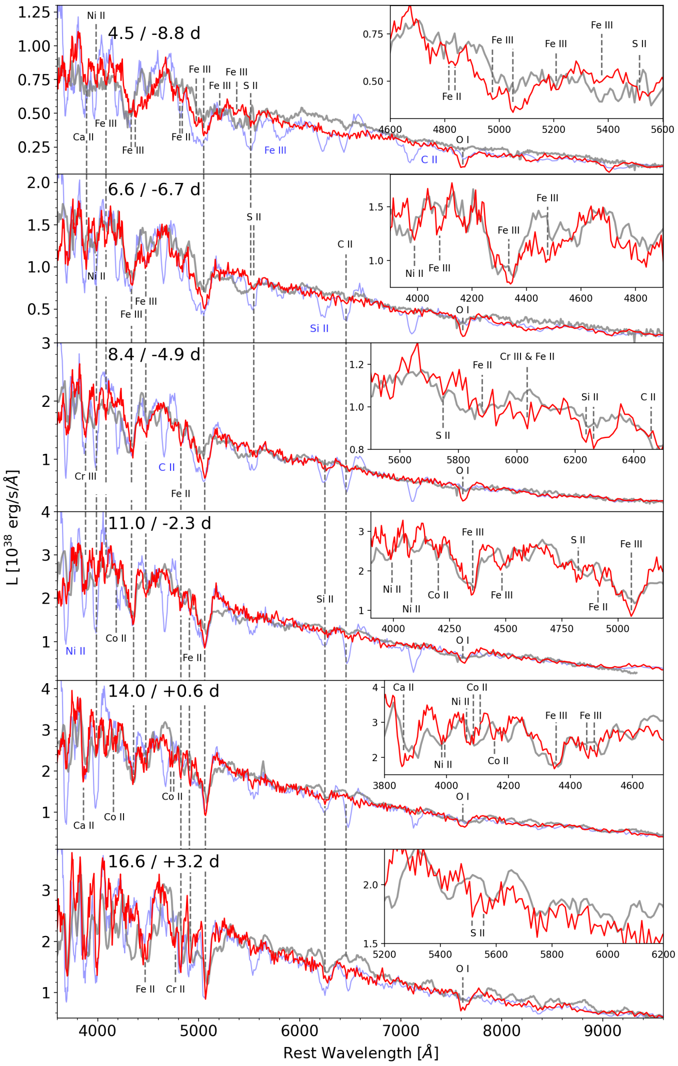

Fig. 2. Early spectral evolution of SN 2024pxl (grey) fitted with the TARDIS synthetic spectra (red) of the the abundance tomography analysis. The unambiguous identification of spectral features based on the TARDIS photon packet statistics are marked with dashed lines. TARDIS spectra calculated by assuming the N1def abundance structure (blue) are also shown for comparison.

centages of carbon mass fraction would form extremely strong features.

Around two weeks after maximum, the Fe II lines start to dominate the optical spectra. The only strong feature formed by another element is the Ca II NIR triplet, while weaker features can be clearly associated with magnesium, chromium, titanium, nickel, and oxygen. Other elements, such as silicon, sulfur, and carbon, do not show any identifiable lines, and the output spectra are relatively insensitive to their mass fractions. According to the fitting strategy described above, these elements are present with constant, N1def-like abundances in the deepest regions of our model.

The relationship between various physical properties and the peak luminosity of SNe Iax has been investigated, including the rise time, Δm_{15}, and photospheric velocities. These studies could not identify any strong correlation, either because of the small sample or the uncertain properties, while the distribution of Δm_{15} parameters even raised the possibility of two populations within the Type Iax class (Singh et al. 2023). In the case of the

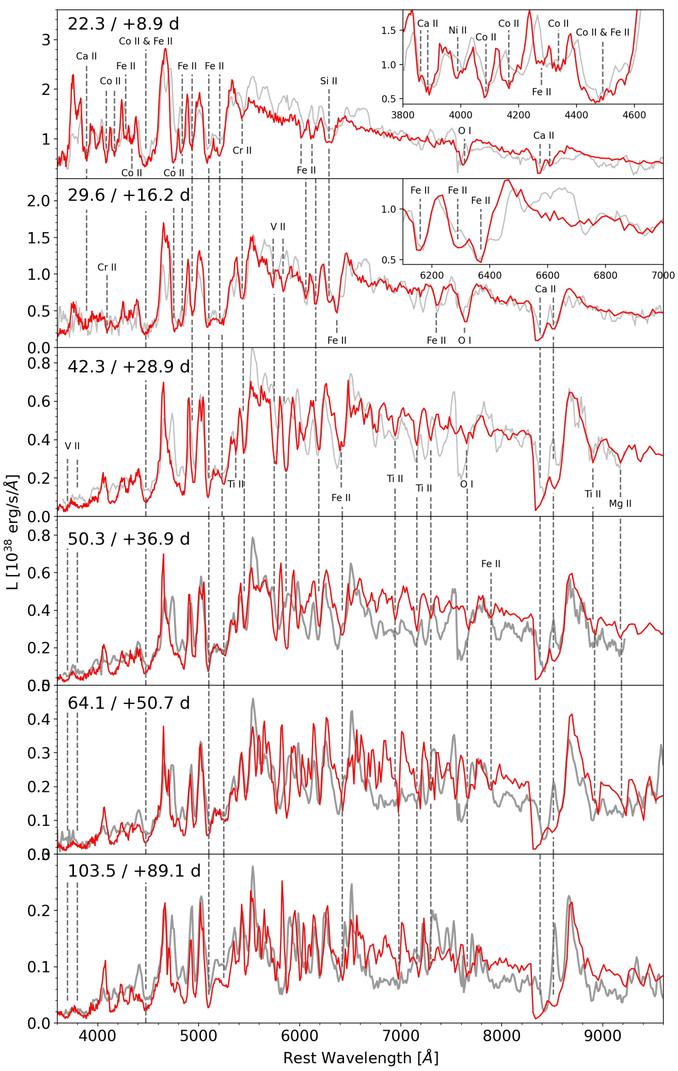

Fig. 3. Late spectral evolution of SN 2024pxl (grey) fitted with the TARDIS synthetic spectra (red) of the the abundance tomography analysis.

photospheric velocity, it can be difficult to accurately measure, due to numerous and overlapping lines as compared to normal SNe Ia. The classical method for thermonuclear SNe is based on the blueshift of the absorption minimum of the prominent and unblended Si II λ6355. For Type Iax SNe, the same feature appears significantly weaker, and it is polluted by Fe II λ6456 even a few days before maximum light. In a few days, the Fe II line dominates the observed P Cygni feature and makes the v_{phot} underestimated due to its longer rest wavelength (Szalai et al. 2015; Maguire et al. 2023). This effect provides an explanation for the scattering of the previously published luminosity-velocity relations and why the measured Doppler-shift of Si II is always lower than that of other elements.

In Bánhidi et al. (2025), the authors suggested that abundance tomography analysis with radiative transfer codes could offer a better measurement for v_{phot}. Reliable spectral synthesis was presented using radiative transfer codes with a sharp blackbody emitting inner ejecta boundary for thermonuclear SNe, implying that the assumption of the photosphere is robust. The naive v_{phot} estimate is based on the line forming region of chemical elements, which starts at the photosphere; thus, the Doppler-shift of the absorption minimum marks its location according to the formation of the P Cygni profiles. In radiative transfer codes like TARDIS, the location of the photosphere influences the density and temperature functions of the model ejecta, which greatly affects the shape of the continuum and the optical depth profiles of every line. Due to the numerous reconstructable lines, the location of the photosphere can be constrained with the precision of a few hundred km s^{-1} at the early and near-maximum epochs. The uncertainty is mainly caused by the poorly constrained moment of explosion since v_{phot} is coupled with t_{exp}. The uncertainty increases later as the strong, saturated features are less sensitive to the photosphere. Even at the latest epochs, a change of v_{phot} by 500 km s^{-1} produced discrepancies that could not be counterbalanced by tuning other parameters. Thus, we can safely assume a general uncertainty of $\pm$500 km s^{-1} for measurements at each epoch of SN 2024pxl.

The v_{phot} values inferred from the tomography analysis are shown in Fig. 6 as a function of t_{exp}. The velocities estimated from the blueshifts of the observed series of the unblended NIR Co II lines (Singh et al. 2026) are also presented for comparison. The difference of $\sim$ 200 km s^{-1} from the values of TARDIS fits between t_{exp} = 20 and 50 days indicates that the region forming the Co II line is indeed linked to the photosphere, providing an independent way to constrain v_{phot} and further validate the tomography method.

4.1. Relation to other SNe Iax

It has been shown in numerous studies that the spectroscopic evolution of SNe Iax is diverse (Magee et al. 2017; Dutta et al. 2022). However, such discrepancies might occur due to the physical properties of the ejecta instead of their chemical composition. In the case of more luminous explosions, higher ejecta masses have been estimated, which is consistent with the predictions of the deflagration models (Fink et al. 2014). The differences are also present in light curves, as less energetic explosions tend to show more rapid evolution, although the correlation is less strong (considering Δm_{15}, Singh et al. 2023) or the estimates of light curve properties are uncertain (Magee et al. 2025, rise time).

In Fig. 1, we compare the spectral evolution of SN 2024pxl with the slightly less energetic Type Iax SNe 2022xlp and 2019muj (M_{r} = $-$16.06 and $-$16.40 mag, respectively), and the more energetic SN 2015H (M_{r} = $-$17.27 mag), at similar epochs. The most obvious difference can be observed at pre-maximum epochs when SN 2019muj shows a steeper continuum flux, which can be interpreted as the result of a hotter photosphere, but could also be the consequence of the uncertain host-galaxy extinctions. At the same time, the observed set of lines is identical, and there are only moderate differences in the relative strength of the spectral features. The agreement between the spectra is even more striking after maximum, when the discrepancies in the continuum and P Cygni profiles almost completely disappear among the three objects. This behavior disfavors the assumption of additional host-galaxy extinction and suggests that SNe Iax with the same peak luminosity have very similar inner properties regarding their temperature, densities, and potentially the continuum source bound remnant. The differences are rather characteristic of the outer ejecta, which also actively shape the light curves before and around maximum light.

In Fig. 6, the photospheric velocities of SN 2024pxl are also compared to those of SNe Iax with either similar peak luminosity or a long coverage of spectral synthesis (Camacho-Neves et al. 2023; Bánhidi et al. 2025). The photospheric evolutions show a similar trend in general: v_{phot} values rapidly decrease first, then the curves continuously flatten after $t_{exp} \simeq 50$ days. All three long-term velocity functions converge to a few hundred km s^{-1}. This feature is a potential clue for the existence of the super-Eddington wind emerging from the bound remnant predicted by the failed deflagration scenario (Foley et al. 2016). Assuming a steady state wind, the v_{phot} = 550 km s^{-1} and $\rho_{phot} = 2.6 \times 10^{-1}$ g cm^{-3} at 100 days indicate a mass-loss rate of $\sim 6 \times 10^{-4}$ M$_\odot$ yr^{-1}. This is almost an order of magnitude lower than the mass loss rate of SN 2014dt ($\sim 4 \times 10^{-3}$ M$_\odot$ yr^{-1}, Camacho-Neves et al. 2023) estimated at a similar epoch.

The interpolated photospheric velocity at the moment of the r band maximum is 4700 km s^{-1}. This value fits perfectly into the trend of SNe Iax shown in Fig. 7, where the peak r band absolute magnitudes are plotted as a function of v_{phot} values estimated for the moment of r band maximum. Here we considered only those SNe Iax that have been the subject of abundance tomography analysis, as the naive method based on the blueshift of P Cygni features, typically that of Si II λ6355, usually underestimates v_{phot} (Szalai et al. 2015; Maguire et al. 2023). The continuity of the luminosity-velocity (L-v) correlation, supported by SN 2024pxl, is an indirect sign of the common origin of the whole Type Iax subclass. Note that the uncertainties of the adopted distances strongly affect the peak absolute magnitudes while also weakly affecting the spectral fits and thus the estimated v_{phot} values. For this reason, we marked those SNe in Fig. 7 that were analyzed based on their relatively uncertain Hubble-flow distance. Due to this and the lack of total coverage over the luminosity range of SNe Iax, the proposed L-v correlation requires further validation.

5. Conclusions

We conducted an abundance tomography analysis on the type Iax SN 2024pxl, one of the most well-observed objects of its subclass. The peak luminosity increases the importance of SN 2024pxl, as it belongs to the small sample of the IL group, and as such, it may provide further insights into the link between the extremities of SNe Iax. The comparison with other SNe Iax with similar peak luminosity revealed practically the same set and shapes of spectral lines but significant differences in the continuum at pre-maximum epochs. This can be interpreted as intrinsic differences in the temperature and/or density profiles of the ejecta or as the result of the uncertain host-galaxy extinctions. Considering the similar inner ejecta properties inferred from the tomography analysis and the lack of spectral discrepancies around three weeks after the explosion, the source of different reddening is probably related to the outer regions of the ejecta.

The tomography analysis is carried out by spectral synthesis performed with the radiative transfer code TARDIS. The described fitting strategy ensures that, despite the large number of free parameters, we can effectively map the properties of the ejecta, including the possible layering of chemical elements. The analysis used the predictions of the single-ignition-point deflagration N1def model, which can effectively describe the ejecta structure of SN 2024pxl based on the line profiles of post-maximum NIR and MIR spectra Kwok et al. (2025), as an initial assumption for the model ejecta. Although the abundance and density structures of the N1def model produced the majority of the existing spectral features, the fit of their line profiles revealed several notable discrepancies. The updates to the abundance structure mainly affected the outermost layers, where both

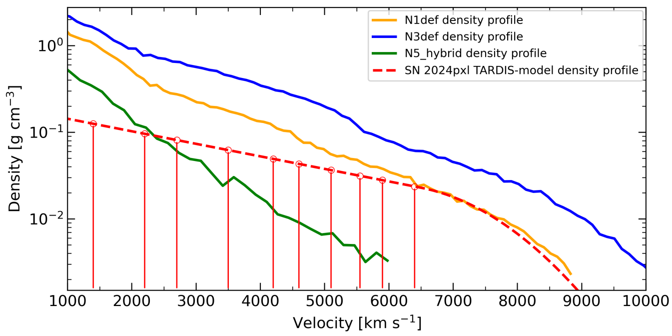

Fig. 4. The assumed density function of the best-matching TARDIS model for SN 2024pxl (red). The density structures of the pure deflagration models with similar peak abosulte magnitudes as SN 2024pxl are also plotted for comparison. The vertical lines show the velocity of the photosphere at the studied epochs.

IMEs and IGEs are present with no or significantly decreased mass fractions in our best-fit model. This region has significantly lower densities than the rest of the ejecta; thus, it mainly affects the earliest spectra, while its impact on the forbidden emission line profiles is insignificant. The stratification of the inferred abundance structure indicates that the mixing of the ejecta after the explosion is not as strong as expected from current pure deflagration models.

The fits of the post-maximum optical spectra are consistent with the assumption that the ejecta are well mixed on large scales, as a constant mass fraction below 4000 km s^{-1} provides the same quality of fitting as stratified solutions. Carbon was identified only in this outer region, but its presence between 4000 and 8000 km s^{-1} would produce overwhelmingly strong carbon features in the early spectra. The carbon abundance is highly ambiguous below 4000 km s^{-1}, since no spectral features were identified during the post-maximum epochs. However, the N1def-like abundance of carbon in the inner region is also consistent with the spectral synthesis. As another significant difference from the predictions of N1def, the densities in the inner layers were decreased by an order of magnitude in our final ejecta model to fit the strong iron features dominating the optical wavelengths.

The photospheric velocity evolution of SN 2024pxl fits well into the sample of SNe Iax. The estimated velocity curves of the SNe show differences according to the absolute magnitudes at the early epochs, as the more energetic explosions expand faster, which provides a strong correlation between v_{phot} values and luminosities at the moment of maximum light. This attribute further supports the idea that SNe Iax originate from a similar explosion mechanism, as there are no breaks or outliers appearing in the IL-region of the velocity distribution. The v_{phot} values match well with those estimated from the Doppler-shift of Co II NIR features, instead of the classical method based on the Si II λ6355 feature (Singh et al. 2026).

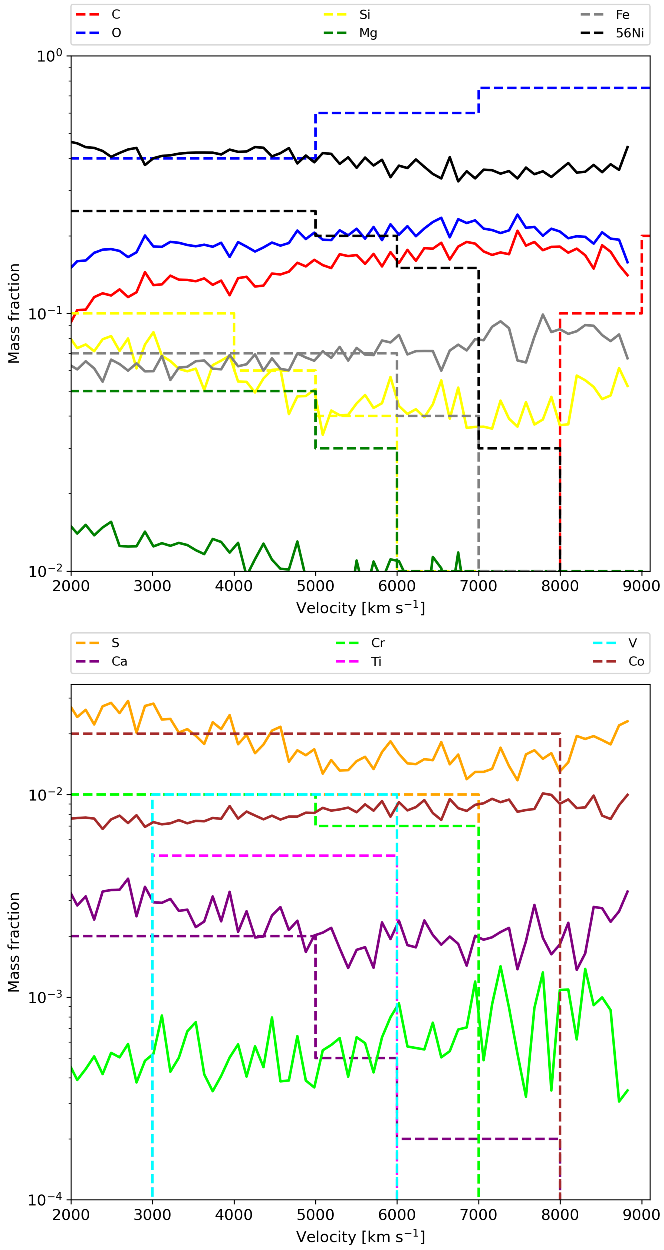

Fig. 5. The mass fractions of chemical elements fitted in the abundance tomography analysis of SN 2024pxl (dashed lines), compared them to those of the N1def pure deflagration model (solid lines).

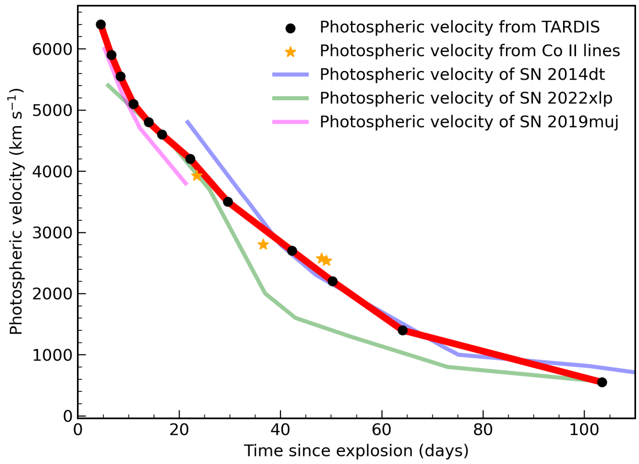

Fig. 6. The photospheric velocity evolution of SN 2014pxl and other SNe Iax with similar absolute magnitude.

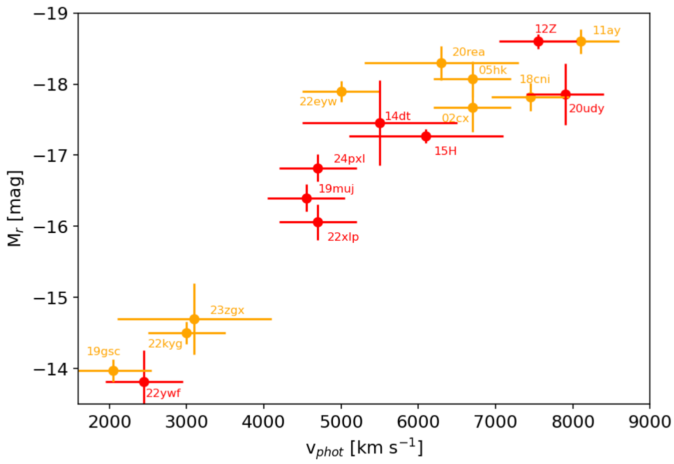

Fig. 7. Absolute magnitudes in r/R-band of SNe Iax as a function of their photospheric velocity at the moment of maximum light. We only plot SNe Iax which have been the subject of abundance tomography. The colors indicate wether the distance of the host galaxy was estimated from the Hubble-flow (orange) or based on any more precise indicators, such as Tully-Fisher relation or SNe (red). In case of no spectral coverage around the maximum (SNe 2014dt, 2015H, and 2023zgx), photospheric velocity is estimated with linear extrapolation and the approximate uncertainty is doubled. The corresponding references are listed in Tab. A.1.

Acknowledgements. This research made use of TARDIS, a community-developed software package for spectral synthesis in supernovae (Kerzendorf & Sim 2014). The development of TARDIS received support from GitHub, the Google Summer of Code initiative, and from ESA's Summer of Code in Space program. TARDIS is a fiscally sponsored project of NumFOCUS. TARDIS makes extensive use of Astropy and Pyne. This work makes use of observations from the Las Cumbres Observatory network. The LCO team is supported by NSF grants AST-2308113 and AST-1911151. Based on observations collected at the European Organisation for Astronomical Research in the Southern Hemisphere, Chile, as part of ePESSTO+ (the advanced Public ESO Spectroscopic Survey for Transient Objects Survey – PI: Inserra). Based on observations collected at the European Southern Observatory under ESO programmes 112.25JQ.012 and 112.25JQ.010. B.B. received support from the Hungarian National Research, Development and Innovation Office grants OTKA PD-147091, the János Bolyai Research Scholarship of the Hungarian Academy of Science and from the HUN-REN Hungarian Research Network. K.M., T.E.M.B. and J.H.T. acknowledge funding from Horizon Europe ERC grant no. 101125877. Time-domain research by the University of Arizona team and D.J.S. is supported by National Science Foundation (NSF) grants 2108032, 2308181, 2407566, and 2432036. L.G. acknowledges financial support from CSIC, MCIN and AEI 10.13039/501100011033 under projects PID2023-151307NB-I00, PIE 20215AT016, CEX2020-001058-M, and by the MaX-CSIC Excellence Award MaX4-SOMMA-ICE. J.H.T. acknowledges Horizon Europe ERC grant no. 101125877. T.-W.C. acknowledges financial support from the Yushan Fellow Program of the Ministry of Education, Taiwan (MOE-111-YSFMS-0008-001-P1), and from the National Science and Technology Council, Taiwan (NSTC 114-2112-M-008-021-MY3). N.F. acknowledges support from the National Science Foundation Graduate Research Fellowship Program under Grant No. DGE-2137419. M.S. acknowledges financial support provided under the National Post Doctoral Fellowship (N-PDF; File Number: PDF/2023/002244) by the Science & Engineering Research Board (SERB), Anusandhan National Research Foundation (ANRF), Government of India. KM acknowledges support from the Japan Society for the Promotion of Science (JSPS) KAKENHI grant (JP24KK0070, JP24H01810, and JP23H04894). Observations from coauthor A.J.M. were made under the aegis of the ASTRAL (Astronomy/STEM Alliance with Lick Observatory) consortium, supported by a generous grant from the Gordon and Betty Moore Foundation (PI B. Macintosh).

References

Ashall, C., Mazzali, P., Bersier, D., et al. 2014, MNRAS, 445, 4427, doi: 10.1093/mnras/stu1995

Ashall, C., Mazzali, P. A., Pian, E., & James, P. A. 2016, MNRAS, 463, 1891, doi: 10.1093/mnras/stw2114

Bánhidi, D., Barna, B., Szalai, T., et al. 2025, A&A, 703, A64, doi: 10.1051/0004-6361/202553922

Barna, B., Szalai, T., Kerzendorf, W. E., et al. 2018, MNRAS, 480, 3609, doi: 10.1093/mnras/sty2065

Barna, B., Szalai, T., Kromer, M., et al. 2017, MNRAS, 471, 4865, doi: 10.1093/mnras/stx1894

Barna, B., Szalai, T., Jha, S. W., et al. 2021a, MNRAS, 501, 1078, doi: 10.1093/mnras/staa3543

Barna, B., Pereira, T., Taubenberger, S., et al. 2021b, MNRAS, 506, 415, doi: 10.1093/mnras/stab1736

Barna, B., Bánhidi, D., Szalai, T., et al. 2026, arXiv e-prints, arXiv:2602.23175, doi: 10.48550/arXiv.2602.23175

Brown, T. M., Baliber, N., Bianco, F. B., et al. 2013, PASP, 125, 1031, doi: 10.1086/673168

Buzzoni, B., Delabre, B., Dekker, H., et al. 1984, Msngr, 38, 9

Camacho-Neves, Y., Jha, S. W., Barna, B., et al. 2023, ApJ, 951, 67, doi: 10.3847/1538-4357/acd558

Das, H., Sahu, D. K., Dutta, A., et al. 2026, ApJ, 999, 10, doi: 10.3847/1538-4357/ae31ed

Dimitriadis, G., Burgaz, U., Deckers, M., et al. 2025, A&A, 694, A10, doi: 10.1051/0004-6361/202451852

Dutta, A., Sahu, D. K., Anupama, G. C., et al. 2022, ApJ, 925, 217, doi: 10.3847/1538-4357/ac366f

Fink, M., Kromer, M., Seitenzahl, I. R., et al. 2014, MNRAS, 438, 1762, doi: 10.1093/mnras/stt2315

Foley, R. J., Jha, S. W., Pan, Y.-C., et al. 2016, MNRAS, 461, 433, doi: 10.1093/mnras/stw1320

Foley, R. J., Chornock, R., Filippenko, A. V., et al. 2009, AJ, 138, 376, doi: 10.1088/0004-6256/138/2/376

Foley, R. J., Challis, P. J., Chornock, R., et al. 2013, ApJ, 767, 57, doi: 10.1088/0004-637X/767/1/57

Graham, M. J., Kulkarni, S. R., Bellm, E. C., et al. 2019, PASP, 131, 078001, doi: 10.1088/1538-3873/ab006c

Hachinger, S., Mazzali, P. A., Taubenberger, S., et al. 2012, MNRAS, 427, 2057, doi: 10.1111/j.1365-2966.2012.22068.x

Hachinger, S., Mazzali, P. A., Sullivan, M., et al. 2013, MNRAS, 429, 2228, doi: 10.1093/mnras/sts492

Harvey, L., Maguire, K., Magee, M. R., et al. 2023, MNRAS, 522, 4444, doi: 10.1093/mnras/stad1226

Hoogendam, W. B., Ashall, C., Jones, D. O., et al. 2025, ApJ, 988, 209, doi: 10.3847/1538-4357/ade787

Jordan, IV, G. C., Perets, H. B., Fisher, R. T., & van Rossum, D. R. 2012, ApJ, 761, L23, doi: 10.1088/2041-8205/761/2/L23

Karambelkar, V. R., Kasliwal, M. M., Maguire, K., et al. 2021, ApJ, 921, L6, doi: 10.3847/2041-8213/ac2e90

Kayal, S., Gayatri, P., Singh, M., & Misra, K. 2025, arXiv e-prints, arXiv:2512.24203, doi: 10.48550/arXiv.2512.24203

Kerzendorf, W., Sim, S., Vogl, C., et al. 2025, tardis-sn/tardis: TARDIS v2025.10.12, release-2025.10.12, Zenodo, doi: 10.5281/zenodo.17330175

Kerzendorf, W. E., & Sim, S. A. 2014, MNRAS, 440, 387, doi: 10.1093/mnras/stu055

Kromer, M., Fink, M., Stanishev, V., et al. 2013, MNRAS, 429, 2287, doi: 10.1093/mnras/sts498

Kromer, M., Ohlmann, S. T., Pakmor, R., et al. 2015, MNRAS, 450, 3045, doi: 10.1093/mnras/stv886

Kwok, L. A., Singh, M., Jha, S. W., et al. 2025, ApJ, 989, L33, doi: 10.3847/2041-8213/adf062

Lach, F., Callan, F. P., Bubeck, D., et al. 2022, A&A, 658, A179, doi: 10.1051/0004-6361/202141453

Leung, S.-C., & Nomoto, K. 2020, ApJ, 900, 54, doi: 10.3847/1538-4357/aba1e3

Li, W., Filippenko, A. V., Chornock, R., et al. 2003, PASP, 115, 453, doi: 10.1086/374200

Long, M., Jordan, IV, G. C., van Rossum, D. R., et al. 2014, ApJ, 789, 103, doi: 10.1088/0004-637X/789/2/103

Magee, M. R., Kotak, R., Sim, S. A., et al. 2016, A&A, 589, A89, doi: 10.1051/0004-6361/201528036

—. 2017, A&A, 601, A62, doi: 10.1051/0004-6361/201629643

Magee, M. R., Killestein, T. L., Pursiainen, M., et al. 2025, MNRAS, 543, 3731, doi: 10.1093/mnras/staf1675

Maguire, K., Magee, M. R., Leloudas, G., et al. 2023, MNRAS, 525, 1210, doi: 10.1093/mnras/stad2316

Mandel, K. S., Thorp, S., Narayan, G., Friedman, A. S., & Avelino, A. 2022, MNRAS, 510, 3939, doi: 10.1093/mnras/stab3496

Mazzali, P. A., Sullivan, M., Hachinger, S., et al. 2014, MNRAS, 439, 1959, doi: 10.1093/mnras/stu077

Mazzali, P. A., Sullivan, M., Filippenko, A. V., et al. 2015, MNRAS, 450, 2631, doi: 10.1093/mnras/stv761

Meng, X., & Podsiadlowski, P. 2014, ApJ, 789, L45, doi: 10.1088/2041-8205/789/2/L45

O'Brien, J. T., Kerzendorf, W. E., Fullard, A., et al. 2024, ApJ, 964, 137, doi: 10.3847/1538-4357/ad2358

Oke, J. B., & Gunn, J. E. 1982, PASP, 94, 586, doi: 10.1086/131027

Oke, J. B., Cohen, J. G., Carr, M., et al. 1995, PASP, 107, 375, doi: 10.1086/133562

Piro, A. L., & Nakar, E. 2013, ApJ, 769, 67, doi: 10.1088/0004-637X/769/1/67

—. 2014, ApJ, 784, 85, doi: 10.1088/0004-637X/784/1/85

Rehemtulla, N., Miller, A. A., Jegou Du Laz, T., et al. 2024, ApJ, 972, 7, doi: 10.3847/1538-4357/ad5666

Sasdelli, M., Mazzali, P. A., Pian, E., et al. 2014, MNRAS, 445, 711, doi: 10.1093/mnras/stu1777

Schlafly, E. F., & Finkbeiner, D. P. 2011, ApJ, 737, 103, doi: 10.1088/0004-637X/737/2/103

Singh, M., Misra, K., Sahu, D. K., et al. 2022, MNRAS, 517, 5617, doi: 10.1093/mnras/stac3059

Singh, M., Sahu, D. K., Dastidar, R., et al. 2023, ApJ, 953, 93, doi: 10.3847/1538-4357/acd559

Singh, M., Sahu, D. K., Barna, B., et al. 2024, ApJ, 965, 73, doi: 10.3847/1538-4357/ad2618

Singh, M., Kwok, L. A., Jha, S. W., et al. 2026, ApJ, 999, 227, doi: 10.3847/1538-4357/ae4318

Smartt, S. J., Valenti, S., Fraser, M., et al. 2015, A&A, 579, A40, doi: 10.1051/0004-6361/201425237

Srivastav, S., Smartt, S. J., Leloudas, G., et al. 2020, ApJ, 892, L24, doi: 10.3847/2041-8213/ab76d5

Stehle, M., Mazzali, P. A., Benetti, S., & Hillebrandt, W. 2005, MNRAS, 360, 1231, doi: 10.1111/j.1365-2966.2005.09116.x

Stritzinger, M. D., Valenti, S., Hoeflich, P., et al. 2015, A&A, 573, A2, doi: 10.1051/0004-6361/201424168

Szalai, T., Vinkó, J., Sárneczky, K., et al. 2015, MNRAS, 453, 2103, doi: 10.1093/mnras/stv1776

Thorp, S., Mandel, K. S., Jones, D. O., Ward, S. M., & Narayan, G. 2021, MNRAS, 508, 4310, doi: 10.1093/mnras/stab2849

Tomasella, L., Stritzinger, M., Benetti, S., et al. 2020, MNRAS, 496, 1132, doi: 10.1093/mnras/staa1611

Tully, R. B., Courtois, H. M., & Sorce, J. G. 2016, AJ, 152, 50, doi: 10.3847/0004-6256/152/2/50

Zimmerman, E. A., Gal-Yam, A., Groot, P. J., et al. 2026, arXiv e-prints, arXiv:2602.09096, doi: 10.48550/arXiv.2602.09096

---

[1] Department of Experimental Physics, University of Szeged, Dóm tér 9, Szeged 6720, Hungary

[2] HUN-REN-SZTE Stellar Astrophysics Research Group, 6500 Baja, Szegedi út, Kt. 766, Hungary

[3] Indian Institute of Astrophysics, Koramangala 2nd Block, Bangalore 560034, India

[4] Center for Interdisciplinary Exploration and Research in Astrophysics (CIERA), 1800 Sherman Ave., Evanston, IL 60201, USA

[5] Department of Physics and Astronomy, Rutgers, the State University of New Jersey,
136 Frelinghuysen Road, Piscataway, NJ 08854-8019, USA

[6] Istituto Nazionale di Astrofisica, Osservatorio Astronomico di Brera, via E. Bianchi 46, 23807 Merate (LC), Italy

[7] Department of Astronomy, University of California, Berkeley, CA 94720-3411, USA

[8] European Southern Observatory, Alonso de Córdova 3107, Vitacura, Casilla 19001, Santiago, Chile

[9] Gemini Observatory/NSF's NOIRLab, 670 North A'ohoku Place, Hilo, HI 96720-2700, USA

[10] Las Cumbres Observatory, 6740 Cortona Drive, Suite 102, Goleta, CA 93117-5575, USA

[11] Department of Physics, University of California, Santa Barbara, CA 93106-9530, USA

[12] Indian Institute of Astrophysics, Koramangala 2nd Block, Bangalore 560034, India

[13] Department of Astronomy and Astrophysics, University of California, Santa Cruz, CA 95064-1077, USA

[14] School of Physics, The University of Melbourne, Parkville, VIC 3010, Australia

[15] Baja Astronomical Observatory of the University of Szeged, Szegedi út, Kt. 766, 6500 Baja, Hungary

[16] Steward Observatory, University of Arizona, 933 North Cherry Avenue, Tucson, AZ 85721-0065, USA

[17] Centro de Astronomía (CITEVA), Universidad de Antofagasta, Av. Angamos 601, Antofagasta, Chile

[18] Institute for Advanced Study in Physics, Zhejiang University, Hangzhou 310027, China

[19] Department of Particle Physics and Astrophysics, Weizmann Institute of Science, 76100 Rehovot, Israel

[20] Graduate Institute of Astronomy, National Central University, 300 Jhongda Road, 32001 Jhongli, Taiwan

[21] Space Telescope Science Institute, 3700 San Martin Drive, Baltimore, MD 21218-2410, USA

[22] Division of Physics, Mathematics and Astronomy, California Institute of Technology, Pasadena, CA 91125, USA

[23] Center for Astrophysics Harvard & Smithsonian, 60 Garden Street, Cambridge, MA 02138-1516, USA

[24] GSI Helmholtzzentrum für Schwerionenforschung, Planckstraße 1, 64291 Darmstadt, Germany

[25] Caltech Optical Observatories, California Institute of Technology, Pasadena, CA 91125, USA

[26] Institute of Space Sciences (ICE, CSIC), Campus UAB, Carrer de Can Magrans, s/n, E-08193 Barcelona, Spain

[27] Institut d'Estudis Espacials de Catalunya (IEEC), E-08034 Barcelona, Spain

[28] Department of Astronomy, Oskar Klein Center, Stockholm University, SE-106 91 Stockholm, Sweden

[29] UCO/Lick Observatory, PO Box 85, Mount Hamilton, CA 95140, USA

[30] Institute of Cosmology and Gravitation, University of Portsmouth, Dennis Sciama Building, Burnaby Road, Portsmouth PO1 3FX, UK

[31] Department of Astrophysics, American Museum of Natural History, Central Park West and 79th Street, New York, NY 10024-5192, USA

[32] Astronomical Observatory, University of Warsaw, Al. Ujazdowskie 4, 00-478 Warszawa, Poland

[33] The NSF AI Institute for Artificial Intelligence and Fundamental Interactions, USA

[34] Department of Physics and Astronomy, University of California, Davis, 1 Shields Avenue, Davis, CA 95616-5270, USA

[35] Department of Physics, Oskar Klein Centre, Stockholm University, SE-106 91, Stockholm, Sweden

[36] Instituto de Astrofísica, Pontificia Universidad Católica de Chile, Av. Vicuña MacKenna 4860, 7820436, Santiago, Chile

[37] Department of Astronomy, University of Virginia, 530 McCormick Rd, Charlottesville, VA 22904, USA

[38] Tuorla Observatory, Department of Physics and Astronomy, FI-20014 University of Turku, Finland

[39] Finnish Centre for Astronomy with ESO (FINCA), FI-20014 University of Turku, Finland

[40] Department of Physics and Astronomy, Northwestern University, 2145 Sheridan Rd, Evanston, IL 60208, USA

[41] Department of Astronomy, Kyoto University, Kitashirakawa-Oiwake-cho, Sakyo-ku, Kyoto, 606-8502. Japan

[42] School of Physics, Trinity College Dublin, The University of Dublin, Dublin 2, Ireland

[43] Research School of Astronomy and Astrophysics, Australian National University, Canberra, ACT 2611, Australia

[44] University of California Observatories, 1156 High Street, Santa Cruz, CA 95064, USA

[45] NSF-Simons AI Institute for the Sky (SkAI), 172 E. Chestnut St., Chicago, IL 60611, USA

[46] Aryabhatta Research Institute of Observational Sciences (ARIES), Manora Peak, Nainital - 263001, India

[47] Instituto de Ciencias Exactas y Naturales (ICEN), Universidad Arturo Prat, Chile

[48] Department of Astronomy, The University of Texas at Austin, 2515 Speedway, Stop C1400, Austin, TX 78712, USA

[49] Department of Physics and Astronomy, The Johns Hopkins University, 3400 North Charles Street, Baltimore, MD 21218, USA

[50] Observatories of the Carnegie Institute for Science, 813 Santa Barbara Street, Pasadena, CA 91101-1232, USA

[51] Department of Physics and Astronomy, Purdue University, 525 Northwestern Avenue, West Lafayette, IN 47907-2036, USA

[52] School of Astronomy and Space Science, University of Chinese Academy of Sciences, Beijing 100049, People's Republic of China

[53] National Astronomical Observatories, Chinese Academy of Sciences, Beijing 100101, People's Republic of China

[54] Department of Astronomy and Astrophysics, University of Chicago, William Eckhart Research Center, 5640 South Ellis Avenue, Chicago, IL 60637, USA

[55] Astrophysics sub-Department, Department of Physics, University of Oxford, Keble Road, Oxford, OX1 3RH, UK

[56] MTA-ELTE Lendület "Momentum" Milky Way Research Group, Hungary

[57] National Astronomical Research Institute of Thailand, 260 Moo 4, Donkaew, Maerim, Chiang Mai 50180, Thailand

[58] Konkoly Observatory, HUN-REN Research Centre for Astronomy and Earth Sciences, MTA Centre of Excellence, Konkoly Thege Miklós út 15-17, Budapest, 1121, Hungary

[59] ELTE Eötvös Loránd University, Institute of Physics and Astronomy, Pázmány Péter sétány 1/A, Budapest, 1117 Hungary

[60] Physics Department and Tsinghua Center for Astrophysics, Tsinghua University, Beijing, 100084, People's Republic of China

Appendix A: Some extra material

Table A.1. The peak absolute magnitudes in r/R-band and photospheric velocities of type Iax SNe at the moment of maximum light.

Supernova	M_r **[mag]**		v_{phot} **[km s^{-1}]**	
SN 2011ay	-18.60	Szalai et al. (2015)	8100	Barna et al. (2017)
SN 2012Z	-18.60	Stritzinger et al. (2015)	7600	Barna et al. (2018)
SN 2020rea	-18.30	Singh et al. (2022)	6300	Kayal et al. (2025)
SN 2005hk	-18.07	Stritzinger et al. (2015)	6700	Barna et al. (2018)
SN 2022eyw	-17.90	Das et al. (2026)	5000	Das et al. (2026)
SN 2020udy	-17.86	Maguire et al. (2023)	7900	Singh et al. (2024)
SN 2018cni	-17.82	Singh et al. (2023)	7500	Singh et al. (2023)
SN 2002cx	-17.67	Li et al. (2003)	6700	Barna et al. (2018)
SN 2014dt	- 17.46	Camacho-Neves et al. (2023)	5500	Camacho-Neves et al. (2023)
SN 2015H	-17.27	Magee et al. (2016)	6100	Barna et al. (2018)
SN 2024pxl	-17.13	Singh et al. (2026)	4700	This work
SN 2019muj	-16.40	Barna et al. (2021a)	4600	Barna et al. (2021a)
SN 2022xlp	-16.06	Bánhidi et al. (2025)	4700	Bánhidi et al. (2025)
SN 2023zgx	-14.70	(Barna et al. 2026)	3100	(Barna et al. 2026)
SN 2020kyg	-14.50	Singh et al. (2023)	3000	Singh et al. (2023)
SN 2019gsc	-13.97	Srivastav et al. (2020)	2100	Srivastav et al. (2020)
SN 2022ywf	-13.81	Barna et al. (2026)	2400	Barna et al. (2026)

Table A.2. The settings and best-matching parameters of the TARDIS model of SN 2024pxl

Physical treatments	
ionization mode	nebular
excitation mode	dilute-lte
radiative rates type	dilute-blackbody
line interaction type	macroatom
Number of photon packets	50000
Number of final pakcets	150000
Iterations	15
Density function	
ρ_0 [g cm^{-3}]	0.2
v_0 [km s^{-1}]	3000
v_{cut} [km s^{-1}]	6500
C	8.2×10^5
Outer velocity boundary	v_{phot} + 5000
T_{exp} [MJD]	60510.6